Liquid-phase Exfoliation of Graphitic Carbon Nitrides Studied by Molecular Dynamics Simulation

Ehsan Shahini[a], Karthik Shankar[b], Tian Tang[a,*]

[a] Department of Mechanical Engineering, University of Alberta, Edmonton, AB T6G 1H9, Canada

[b] Department of Electrical and Computer Engineering, University of Alberta, Edmonton, AB T6G 1H9, Canada

[*] Corresponding author. Tel: 780-492-5467. E-mail: ttang1@ualberta.ca (Tian Tang)

Abstract

Hypothesis

The superiority of graphitic carbon nitride (g-C_3N_4) nanosheet results from its large specific surface area, which can be achieved by exfoliation of the bulk layered structure. Liquid-phase exfoliation (LPE) is the best-known method for the synthesis of two-dimensional (2D) g-C_3N_4 nanosheets. However, experimental investigations do not allow for a molecular-level understanding of the process. Molecular dynamics (MD) simulations are expected to provide microscopic insights and quantitative evaluation of the energy consumption during LPE, thus facilitating the search of effective solvents for the LPE of 2D materials.

Simulations

MD simulations are carried out to simulate the LPE process by performing potential of mean force calculations for the separation of two stacked g-C_3N_4 nanosheets. Free energy of exfoliation is evaluated and compared among nine common solvents with distinct molecular structures.

Findings

The most probable path for the exfoliation process is identified. The free energy of exfoliation is found to correlate directly with the solvent free energy of a single g-C_3N_4 nanosheet. The solvation is enthalpy-driven and affected by the mobility of the solvent molecules around the nanosheet. Based on the MD results, several strategies are proposed to guide the selection of solvents for effective LPE.

Keywords

Graphitic carbon nitride, Liquid-phase exfoliation, 2D materials, Free energy of exfoliation, Solvation free energy

1. Introduction

Two-dimensional (2D) graphitic carbon nitride (g-C_3N_4) nanosheets have been explored as a promising candidate in many applications such as photocatalysis [1–4], membranes [5], sensing [6], imaging [7], and energy conversion [8,9]. Importantly, the basic structural unit of g-C_3N_4 is a π-conjugated heptazine or triazine, which exhibits special electronic and photocatalytic performances [10]. In addition, a weaker photoluminescence intensity was observed in ultrathin g-C_3N_4 nanosheets compared to the layered bulk material [3], which corresponds to a lower inter-sheet recombination rate of photogenerated carriers. Therefore, the superiority of ultrathin g-C_3N_4 sheets results from a large specific surface area, enhanced electron transport ability, and high charge separation efficiency [11]. Liquid-phase exfoliation (LPE), as an important functional modification strategy, can be used to delaminate layered g-C_3N_4 bulk material to obtain free-standing nanosheets [12–18]. In this process, bulk materials are placed into certain solvents followed by ultrasonic treatments [19]. Despite some successes [20–27], it remains a challenge to identify solvents that enable effective exfoliation and stable dispersion of the g-C_3N_4 sheets.

A number of studies have investigated the delamination of bulk g-C_3N_4 in different organic solvents. The selection of solvents was mostly arbitrary, based on trial-and-error experimentation. For example, Yang et al. reported LPE of bulk g-C_3N_4 using various organic solvents as the dispersion medium, including but not limited to isopropanol (IPA), N-methyl-pyrrolidone (NMP), acetone (ACE), and ethanol [28]. It was found that NMP was a promising solvent, which could stabilize the individual nanosheets. In comparison, precipitation of g-C_3N_4 was observed after 2 days when using ethanol and ACE. Lin et al. reported a mixed solvent approach for the LPE of bulk g-C_3N_4, to form monolayer g-C_3N_4 nanosheets with tunable concentrations (0.1−3 mg mL^{-1}) [29]. Different binary solvents, namely ethanol/H_2O, IPA/H_2O, and dimethylformamide (DMF)/H_2O were examined. For the ethanol/H_2O system, when the volume ratio of H_2O was 75%, a milky dispersion was obtained, reaching the maximum g-C_3N_4 concentration of 3 mg mL^{-1}.

To the best of our knowledge, attempts to determine a quantitative relationship between the solvent properties and the performance of the exfoliation are completely absent for g-C_3N_4, while there has been some work on another 2D material, graphene. Hernandez and co-workers [21] reported that the Hildebrand solubility parameters, Hansen solubility parameters, and surface tensions may be used to identify solvents that are effective in dispersing graphene. It was discussed that in order

to minimize the enthalpic cost of mixing, efficient solvents should have a surface tension close to that of graphene. In another study, Coleman et al. [30] stated that the concentration of dispersed graphene nanosheets is maximized when the energy of exfoliation is minimized. An equation was proposed to calculate the enthalpy of mixing ΔH_{mix} as an estimate for the energy of exfoliation,

$$\frac{\Delta H_{mix}}{V_{mix}} = \frac{2}{T_{sheet}}\left(\sqrt{E_{sur}^{graphite}} - \sqrt{E_{sur}^{solvent}}\right)^2 \emptyset \quad (1)$$

where V_{mix} is the volume of the solution mixture, T_{sheet} is the thickness of a nanosheet, E_{sur}^{i} is the surface energy of component *i*, and $\emptyset$ is the volume fraction of graphene in the solution.

The above semiempirical criteria have provided some general guidelines for solvent selection, however, they do not allow for molecular-level design of novel solvents capable of effectively dispersing 2D nanosheets, especially g-C_3N_4. For example, an effective solvent should have interactions with g-C_3N_4 that are strong enough to compensate for the van der Waals (vdW) attraction between the g-C_3N_4 sheets. It is unclear whether these interactions can be captured by solubility parameters or surface tension alone. In this regard, little is known about the molecular details of the interactions between g-C_3N_4 and solvent molecules, and the correlation of these interactions with the structural properties of the solvents. Hence, developing a molecular-level understanding of the interactions between g-C_3N_4 and common solvents can provide fundamental insights that help the design of exfoliation strategies to obtain stable g-C_3N_4 solutions.

Molecular dynamics (MD) is a powerful numerical tool that can shed light on interactions beyond the accessibility of current experimental techniques. Zou et al. [31] presented the first MD study on the exfoliation of g-C_3N_4 nanosheets, where an external force was added to imitate the sonication process. The energy barrier for exfoliation was estimated by the variation of kinetic energies in MD simulations, which was a very rough approximation. There was a lack of accurate evaluation of the free energy required in the exfoliation process, as well as elucidation on the relationship between the free energy and solvent properties. In this work, we present a systematic MD study on the LPE of g-C_3N_4 in nine different solvents with varying molecular structures. Through potential of mean force (PMF) calculations, we have for the first time quantified the free energy of exfoliation between two g-C_3N_4 sheets, which can be used as a metric to evaluate the performance of g-C_3N_4 exfoliation in those solvents. Mechanistic explanations are provided on the relationship between the free energy of exfoliation and molecular features of the solvent. Results

from this study shed light on how to make molecular structure-based selection of solvents to improve g-C_3N_4 exfoliation and dispersion in the liquid-phase.

2. COMPUTATIONAL DETAILS

2.1. Molecular models for g-C_3N_4 and solvents

The heptazine-based g-C_3N_4 nanosheet was considered for this study (Figure 1a). This structure consists of 6-membered rings with sp^2 bonds between C and N atoms, and intrinsically contains vacancies (or voids) surrounded by nitrogen atoms as shown by the red circle in Figure 1a. The presence of these vacancies and the rotation at the N-C bonds that connects two building blocks (cyan circle in Figure 1a highlights one building block) make the growth of a large-sized layer difficult [20]. In this work, we considered an equilateral triangular sheet to be representative of a g-C_3N_4 nanosheet, consistent with several previous studies [32–36], with a side length of 4.5 nm. This nanosheet consists of 21 heptazine core units, with the periphery saturated with 21 H atoms. The justification for choosing this size is provided in Supporting Information (SI), section 1.

For the study of LPE, nine solvents commonly used in the experiments [27,29,37] were considered as the medium. These solvents were categorized into three groups based on their structural character and functional groups. The first group (Figure 1b) featured polar O-H (hydroxyl) groups and included water and two alcohols: methanol (MET) and 1,4-butanediol (BD). The second group (Figure 1c) had a carbonyl (O=C) group which can be an amide as in formamide (FRM) and dimethylformamide (DMF), or a ketone as in ACE. The third group (Figure 1d) contained an aromatic structure: a benzene ring in chlorobenzene (CB), or a heterocycle in tetrahydrofuran (THF) and N-methyl-2-pyrrolidone (NMP).

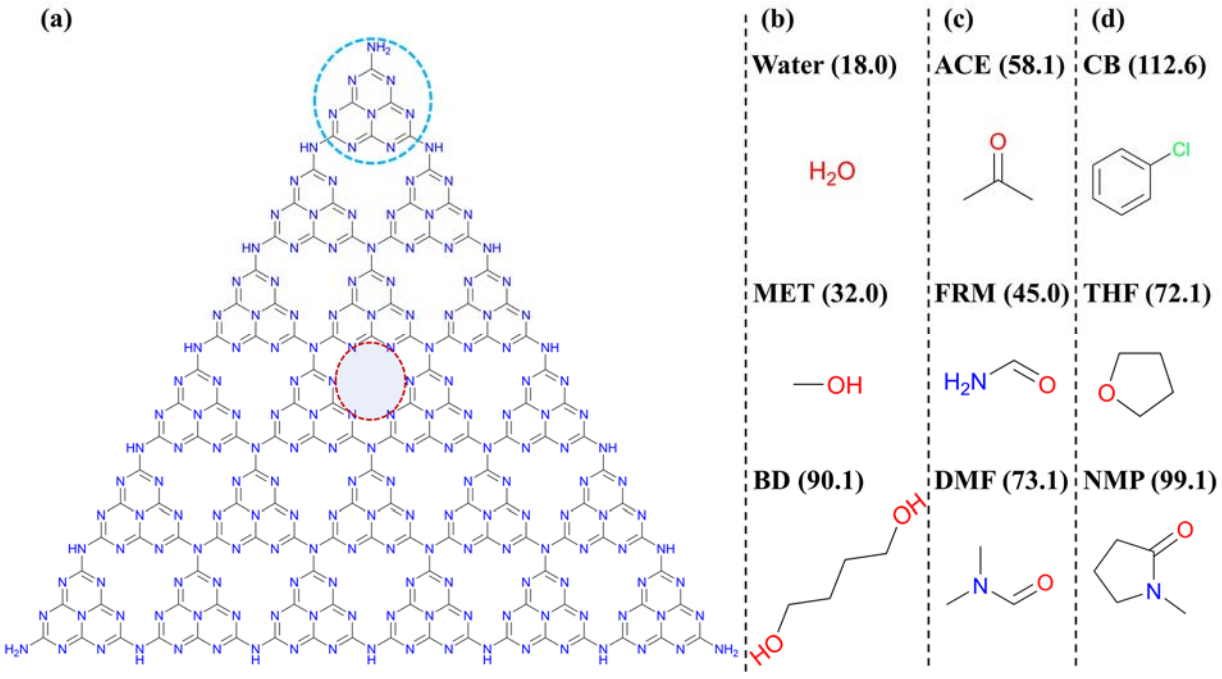

Figure 1. (a) Molecular structure of the 21-unit g-C_3N_4 used in this study. The cyan circle shows one heptazine core unit and the red circle shows a vacancy that exists around the N atoms. Molecular structures of simulated solvents, categorized into group 1 (b), group 2 (c) and group 3 (d) according to their structural characteristics. The molar weight of each solvent is given in the parenthesis.

The all-atom optimized potentials for liquid simulations (OPLS-AA) force field [38] was used for both the solute (g-C_3N_4) and the solvents. The force field parameters were generated from LigParGen and PolyParGen servers [39,40] unless otherwise specified. The Charge Model 5 (CM5) with a scaling factor of 1.20 [41] was used for the partial atomic charges. To validate the force field parameters and partial atomic charges, key properties of g-C_3N_4 such as bond length/angle distributions, surface energy and hydration free energy were compared with results from density functional theory (DFT) calculations. Validation was also performed for the solvents, by comparing their density, dielectric constant, and surface tension with experimental results. Details of the validation are shown in the SI, Section S2.

2.2. Simulated systems

Umbrella sampling (US) [42] was used to calculate the PMF, which is defined as the potential whose negative gradient with respect to a pre-defined reaction coordinate (RC) corresponds to the

average force in the direction of the RC. The weighted histogram analysis method (WHAM) [43] was used to extract the PMF curve from a set of US simulations. It is non-trivial to define a RC that best describes the exfoliation of the g-C_3N_4 nanosheets. Two adhered 2D sheets can be separated via different paths, which may be associated with different free energy requirements [44–48]. For example, it was shown that for graphene sheets in water the PMF to separate them in the direction perpendicular to the sheets (i.e., normal direction) was lower compared to that in the direction parallel to the sheets (i.e., lateral direction) [45]. However, for boron nitride (BN) nanosheets in several organic solvents, it was reported that the lateral direction had lower PMF [46].

In this work, we first performed a set of simulations to determine the most probable path for the exfoliation of g-C_3N_4. For this purpose, three different RCs were explored with DMF being the solvent. RC I was defined as the distance between the centers of mass (COMs) of two sheets along the normal direction (Figure 2a); PMF associated with this RC corresponded to the process of separating the two sheets in the normal direction. RC II was the distance between the edge atoms of two sheets in the normal direction (Figure 2b), resembling the peeling of the top sheet from the bottom one. Finally, RC III was the distance between the COMs of two sheets in the lateral direction (Figure 2c), to capture the process of sliding the top layer over the bottom one. RC I ranged from 0.3 to 1.3 nm, beyond which the two sheets no longer interacted with each other, while RC II and III ranged from 0.3 to 4.0 nm. For each chosen RC, US simulations were performed by applying a harmonic biasing potential (force constant 5000 kJ/mol.nm^2) to restrain the RC at each US window. To complement the PMF calculations, a pulling simulation was carried out along each of the three RCs in DMF. In these simulations, the bottom sheet was fixed while the center of the mass (COM) of the top sheet (RC I and RC III) or edge atom (RC II) of the top sheet was attached to a spring of stiffness 1000 kJ/mol.nm^2 and pulled away at a speed of 0.005 nm/ps. PMFs and forces obtained from the three RCs were compared to determine the one with the lowest resistance to separation, i.e., the most probable path for exfoliation. Then this RC was employed to calculate the PMFs for all the other solvents.

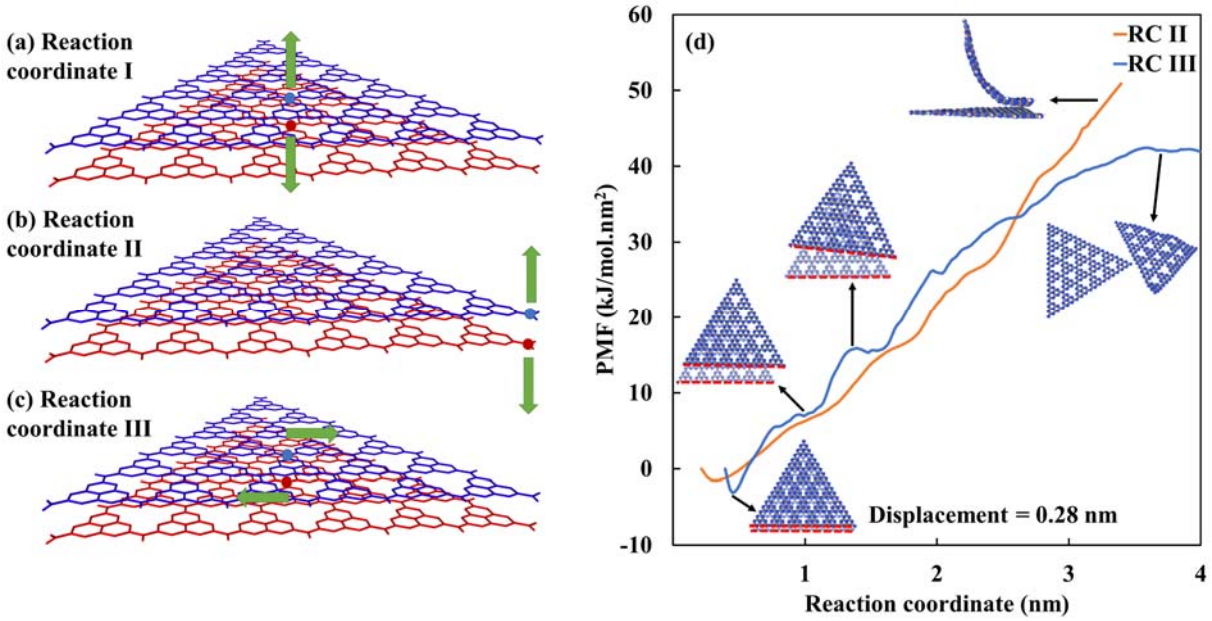

Figure 2. Three RCs explored for the separation of two g-C_3N_4 nanosheets: (a) the distance between the COMs of two sheets along the normal direction, (b) the distance between the edge atoms of two sheets in the normal direction, and (c) the distance between the COMs of two nanosheets in the lateral direction. For better illustration, the two sheets are colored differently. The COMs or edge atoms are shown with blue and red circles respectively for the two sheets. (d) PMF curves for separating two stacked g-C_3N_4 nanosheets in DMF along RC II and RC III. Insets show representative snapshots at different stages of the separation.

In addition to the PMF calculations, a set of simulations were performed to determine the solvation free energy (SFE, denoted by ΔG_{sol}) of a single g-C_3N_4 sheet in different solvents. Bennett Acceptance Ratio (BAR) method [49] was used to gradually couple a sheet to its equilibrium solvation environment and the average $\langle dH(\lambda)/d\lambda \rangle$ was evaluated, where H is the Hamiltonian and λ is the coupling parameter. Twenty-one states were defined in this procedure where the first state corresponded to no interaction ($\lambda = 0$) between the g-C_3N_4 sheet and the solvent. In the next 10 states the vdW interaction between the g-C_3N_4 sheet and the solvent was increased with the step of $\Delta\lambda = 0.1$. For the last 10 states the electrostatic interaction was turned on by the step of $\Delta\lambda = 0.1$ reaching the fully interacting state between the sheet and solvent. Consequently, the ΔG_{sol} between $\lambda = 0$ and $\lambda = 1$ can be calculated from:

$$\Delta G_{sol} = \int_{\lambda=0}^{\lambda=1} \langle \frac{dH}{d\lambda} \rangle_{\lambda} \, d\lambda \quad (2)$$

Finally, the fully interacting systems from the end of the ΔG_{sol} simulations were further equilibrated for 60 ns. Afterward, the g-C_3N_4 sheet was removed from each system, the solvent was re-equilibrated for 60 ns and the g-C_3N_4 sheet was equilibrated in vacuum for 10 ns. This set of simulations allowed us to calculate the solvation enthalpy (ΔH_{sol}) from

$$\Delta H_{sol} = H_{solution} - H_{solvent} - H_{solute} \quad (3)$$

where $H_{solution}$ is the enthalpy of the solution after 60 ns equilibration, $H_{solvent}$ is the enthalpy of the solvent alone after 60 ns re-equilibration, and H_{solute} is the enthalpy of the sheet alone after 10 ns equilibration in vacuum. Each enthalpy term was calculated based on $H = E + pV$ where E is the internal energy, p is pressure and V is volume. The solvation entropy was then estimated by

$$T\Delta S_{sol} = \Delta H_{sol} - \Delta G_{sol} \quad (4)$$

where T = 300 K is the simulation temperature. A summary of the simulated systems is given in Table 1. These simulations generated trajectories with a total length of 5 μs.

Table 1. Summary of the simulated systems.

Simulation type	# g-C_3N_4 sheets	Solvent	Size of the box (nm*nm*nm)	# simulation windows	Time of production run in each simulation window (ns)
Pulling	2	DMF	9*10*9	1	1
PMF with RC I	2	DMF	8*8*10	40	10
PMF with RC II	2	DMF	8*8*10	30	10
PMF with RC III	2	Water, MET, BD, ACE, FRM, DMF, CB, THF, NMP	9*10*9	40	10
ΔG_{sol} calculation	1	Water, MET, BD, ACE, FRM, DMF, CB, THF, NMP	7*7*4	21	1
ΔH_{sol} and ΔS_{sol} calculation	0 and 1	Water, MET, BD, ACE, FRM, DMF, CB, THF, NMP	5.8*5.8*5.8	1	60

2.3 Simulation details

All simulations were performed using the GROMACS package [50] (version 2021.2). Prior to each production run, energy minimization of the system was carried out using a steepest descent

algorithm. The system was then equilibrated in the NpT ensemble for 200 ps with a 2 fs timestep. The temperature and pressure were controlled at 300 K and 1 bar by the Berendsen thermostat and barostat, with a coupling time constant of 0.2 ps and 5 ps respectively. A production run was subsequently performed with a 2 fs timestep, where the bond lengths involving a hydrogen atom were constrained using the LINCS algorithm. A temperature of 300 K was maintained by means of a velocity-rescale algorithm with a time constant of 0.1 ps. An isotropic pressure of 1 bar was set by using a C-rescale scheme with a coupling constant of 1.0 ps. Periodic boundary condition was employed in all directions, and long-range electrostatic interaction was evaluated using the particle-mesh Ewald summation. The cutoff radius for the nonbonded interactions was set to 1.2 nm. The length of each production simulation is given in Table 1.

3. Results and discussion

3.1. Selection of reaction coordinate

To determine the most probable path for exfoliation, pulling simulations for two stacked g-C_3N_4 sheets in DMF were first performed for all three RCs. The force-displacement curves are shown in SI, Section S3. Along RC I a large force (~ 4300 kJ/mol·nm) is required, which occurs at around 0.45 nm, in order to overcome the π-π interaction [51] between the two stacked sheets. After this peak, the force decreases rapidly because of the diminishing interactions. For RC II and III, the force is steady and below ~1000 kJ/mol·nm. The results suggest that exfoliation via RC I is significantly more difficult compared with RC II and III as demonstrated by the more than 4-fold larger force required at the initial stage. Subsequently, we focused on RC II and III and generated the associated PMF curves in Figure 2d. Here the dimension of the PMF is energy per unit area (normalization done using the area of one nanosheet), and the PMF value of the first data point was set to zero in both curves. At the early stage (RC < 2.5 nm), the two PMFs are comparable. However, as the RC further increases, the two curves show the sign of separating from each other. When RC > 3.0 nm, the curve for RC III has leveled off while the one for RC II curve is still climbing. The difference between the two curves can be understood by recognizing that while the separation of the two nanosheets, and hence the loss of interaction between them, is gradual at the beginning for both RCs, in the final stage detaching the top sheet from the bottom one along RC II (inset of Figure 2d) requires a much larger amount of energy. These results suggest that among the three RCs, RC III requires the least amount of energy to completely separate two stacked g-

C_3N_4 sheets, and therefore exfoliation in the experiments is more probable to occur along this RC. The same observation is also confirmed numerically in other solvents (CB and NMP, see SI section S3), and for other 2D materials such as BN [46]. For this reason, PMF calculations were performed along RC III for all 9 solvents and compared to assess their ability to disperse g-C_3N_4 sheets.

3.2. PMF and free energy of exfoliation

The PMF curve in DMF associated with RC III (blue curve in Figure 2d) is examined with details here. As the COM distance (D) between the two sheets increases, the PMF shows an initial decreasing trend, characteristic of a repulsive interaction between them. The curve reaches the global minimum at D = 0.45 nm where the average force between the two sheets is zero. At the global minimum, the sheets are stacked with a lateral shift of 0.28 nm (inset of Figure 2d) compared to the initial configuration where they are in complete overlap. This configuration has been predicted for both g-C_3N_4 [52] and graphene like C_3N [53] bilayers by DFT calculations and corresponds to displaced π–π stacking. After the global minimum, the PMF exhibits an overall increasing trend, which represents attraction between the two sheets. There are small fluctuations in the curve, and the local minima and maxima are caused by the triangle patterns in the g-C_3N_4 structure. Specifically, the heptazine core units from the two sheets prefer to be overlapping with each other, and the same applies to the void regions. Occurrence of such a configuration tends to result in a local minimum in the PMF. For example, the inset of Figure 2d at D = 1.15 nm shows the structure of two nanosheets that have ten of their heptazine core units overlapped. On the contrary, at D = 1.25 nm (inset of Figure 2d), the heptazine core units are not aligned, leading to a local maximum in the PMF curve. The PMF curve reaches a plateau around D = 3.50 nm, indicating negligible interaction between the sheets beyond this COM separation. The difference in PMF value between the global minimum and the plateau represents the free energy required to separate two stacked sheets, via the mode of sliding, from their equilibrium distance until they are no longer interacting. This difference is therefore defined as the free energy of exfoliation (ΔG_{exf}, positive throughout this work).

The PMF curves for all 9 simulated solvents are presented in Figure 3a, with ΔG_{exf} marked for DMF as an example. Validity of the ΔG_{exf} calculation is demonstrated by good overlaps between the US histograms as well as reproducibility confirmed by five independent set of US simulations performed for DMF (SI, Section S3). Quantitatively, ΔG_{exf} measures the level of difficulty to

exfoliate one sheet from another; lower ΔG_{exf} is preferred and exfoliation is expected to be easier with less external efforts (e.g. ultrasonication time and intensity) required. The ranking of ΔG_{exf} follows: water > MET > FRM > ACE > BD > THF > CB > DMF > NMP, which suggests that exfoliation of g-C_3N_4 is easiest in DMF and NMP, and hardest in water.

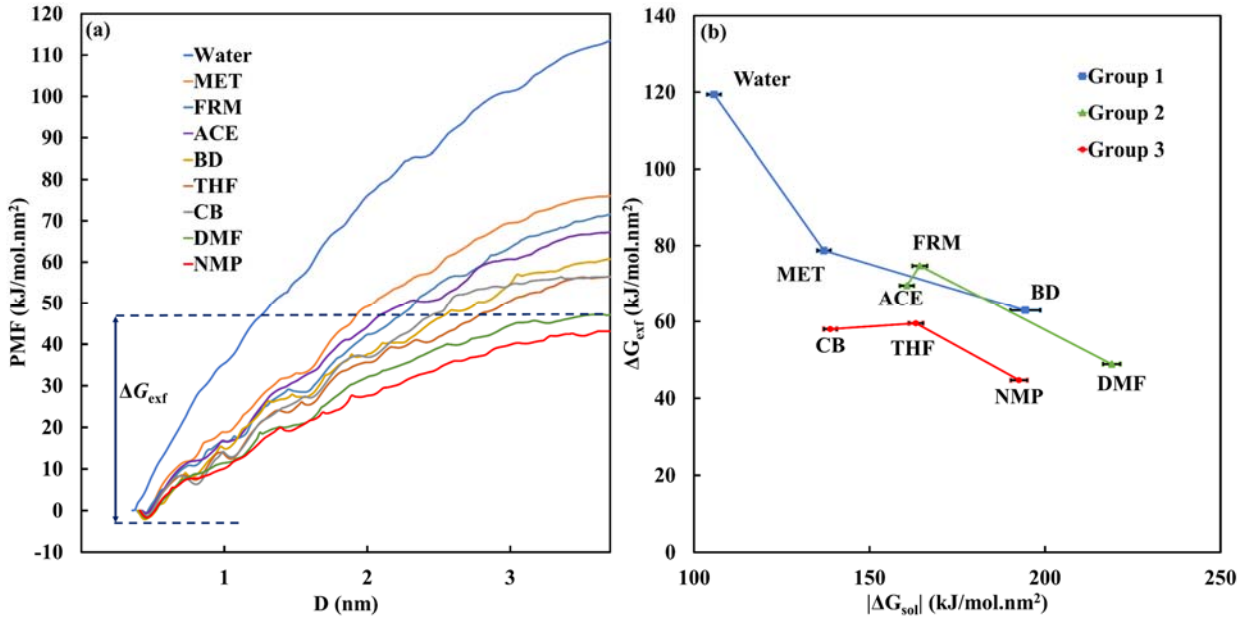

Figure 3. (a) PMF curves for separating two g-C_3N_4 nanosheets in all solvents investigated in this study. (b) ΔG_{exf} vs. $|\Delta G_{sol}|$ for solvents from the three groups. Error bars in $|\Delta G_{sol}|$ are obtained by splitting the data into 5 blocks, calculating the free energy difference over each block, and estimating the error from the average variance over the blocks [54].

3.3. Mechanisms governing the free energy of exfoliation

While the PMF calculations have allowed us to evaluate and rank the free energy of exfoliation, mechanisms behind such ranking require more investigation. Fundamentally, stronger attractive interaction between g-C_3N_4 and the solvent should lead to better solubility and a lower value of ΔG_{exf}, and this was demonstrated for graphene oxide nanosheets [55]. Quantitatively, the solubility can be evaluated by calculating the SFE (ΔG_{sol}) of a single sheet, which is the energy required to create a unit area of contact between the g-C_3N_4 sheet and the solvent. ΔG_{sol} is negative for all solvents, indicating attractive interaction between the sheet and the solvent. ΔG_{exf} is plotted against $|\Delta G_{sol}|$ in Figure 3b for all three groups of the solvents. The standard deviation in $|\Delta G_{sol}|$ is small; hence hereafter we will refer only to the average values. In general, a negative correlation between

ΔG_{exf} and $|\Delta G_{sol}|$ is observed within each group, consistent with our expectation that better solubility would lead to easier exfoliation. The three groups are examined in more detail to identify how the structural features of the solvent molecules affect ΔG_{sol}, and hence ΔG_{exf}.

3.3.1 Group 1 (solvents with hydroxyl group):

In this group the ranking for $|\Delta G_{sol}|$ follows BD > MET > water which suggests BD as a better liquid for the exfoliation of g-C_3N_4. Interestingly, the size and molecular weight (MW) of the solvents in this group follow the same trend, BD (90.1) > MET (32.0) > water (18.0). A few analyses were done to further investigate the relationship between ΔG_{sol} and structural features of the solvent molecules. Because all three solvents in this group contain hydroxyl groups capable of forming hydrogen bonds (H-bonds), an analysis was first performed to calculate the number of H-bonds dissociated and generated during the solvation. The results are provided in SI, Section S4, which show no direct correlation with ΔG_{sol}. In fact, larger size of MET and BD molecules has limited their capability to orient themselves in order to form close contact with the interior of the sheet. The solvent-sheet interaction is therefore suspected to be more impacted by non-specific electrostatic and vdW forces. In addition, entropy may play an important role in solvation [56]. In the following, ΔG_{sol} is separated into its enthalpic and entropic components to gain more insights into the governing contribution.

ΔG_{sol} and its partition into the enthalpic (ΔH_{sol}) and entropic ($T\Delta S_{sol}$) terms are given in SI, Section S5. Both ΔH_{sol} and $T\Delta S_{sol}$ are negative, suggesting that solvation of the nanosheet in the three solvents is favored by enthalpy while opposed entropically. In addition, the magnitude of ΔH_{sol} is more than double that of $T\Delta S_{sol}$, and the magnitudes of ΔH_{sol} and ΔG_{sol} follow the same order of BD > MET > water. The solvation of the nanosheet is therefore an enthalpy-driven process, larger reduction in enthalpy indicates higher sheet-solvent affinity, and leads to more favorable exfoliation [44,46,57,58].

Solvation of a g-C_3N_4 nanosheet involves multiple steps with different energy implications. First, a cavity must be created in the solvent to accommodate the sheet. This step is both entropically ($\Delta S < 0$) and enthalpically ($\Delta H > 0$) unfavorable, as it increases the order of the solvent and reduces solvent-solvent interaction. Stronger interaction among solvent molecules leads to a greater enthalpic penalty for cavity formation. Next, the sheet enters the cavity, and the resulting solvent-sheet interaction is enthalpically favorable ($\Delta H < 0$). Finally, as the solute is mixed into the solvent,

there is an entropy gain ($\Delta S > 0$). Since the solvation of g-C_3N_4 nanosheet is enthalpy driven, we further calculated the energy changes during these steps. The energy change associated with creating a cavity in the solvent, denoted by ΔE_1, was estimated from the difference in non-bonded interactions (vdW and electrostatic) among the solvent molecules from two 60 ns simulations (last set in Table 1): one with the presence of a sheet and one without the sheet. Similarly, the energy change due to the insertion of a sheet into a pre-existing cavity, denoted by ΔE_2, was estimated from the non-bonded interactions between the solvent and the sheet after 60 ns equilibration of the sheet in the solvent. The total energy change in the solvation process then can be estimated as

$$\Delta E = \Delta E_1 + \Delta E_2 \quad (5)$$

Figure 4a shows ΔE_1, ΔE_2, ΔE along with ΔH_{sol} from SI, Section S5. Statistics are based on the last 30 ns of the two 60 ns simulations described above. ΔE and ΔH_{sol} only differ by a small amount suggesting that non-bonded interactions are the main contribution to the enthalpy of solvation. From Figure 4a, the penalty for disrupting solvent-solvent interaction (ΔE_1, positive) follows order of water > BD > MET. Meanwhile, attractive solvent-sheet interaction (ΔE_2, negative) follows water > MET > BD. Solvating the nanosheet in water involves both higher penalty for disrupting solvent-solvent interaction and weaker solvent-sheet attraction, consistent with its smallest $|\Delta G_{sol}|$ and highest ΔG_{exf}. While ΔE_1 is higher in BD than in MET, it is compensated by the stronger attraction between BD and the sheet, making BD a better medium for g-C_3N_4 solvation.

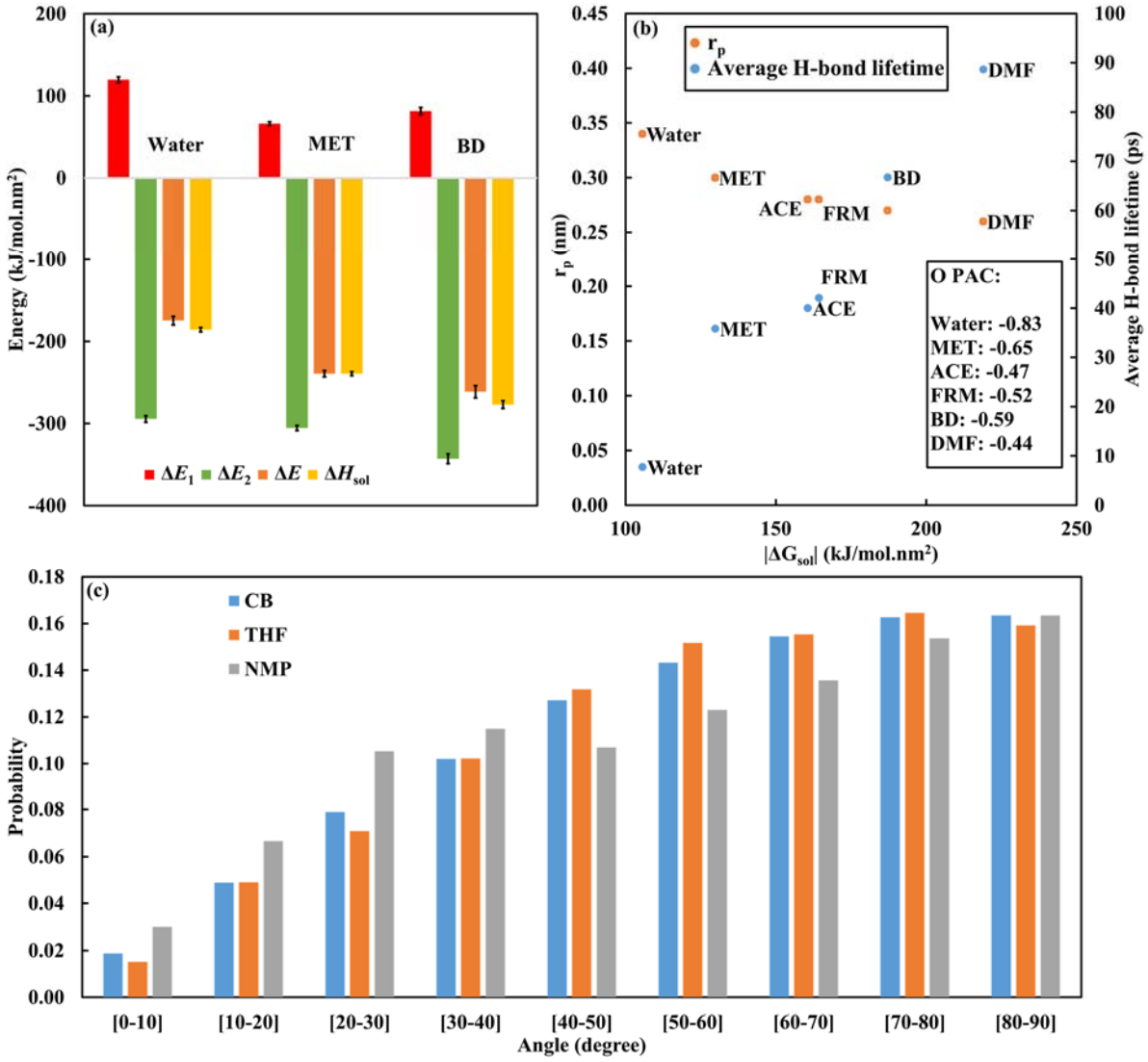

Figure 4. (a) For group 1 solvent: energy changes in the solvation process associated with cavity generation (ΔE_1) and sheet insertion (ΔE_2). The sum of the two terms ($\Delta E = \Delta E_1 + \Delta E_2$) along with ΔH_{sol} are also shown. (b) For group 1 and 2 solvents: r_p (location of the first peak in the RDF) vs. $|\Delta G_{sol}|$ (left axis) and average H-bond lifetime vs. $|\Delta G_{sol}|$ (right axis) for group 1 and 2 solvents. Inset shows the partial atomic charges (PAC) of the solvent oxygen. (c) For group 3 solvents: probability distribution of the angle between the normal of the sheet and the normal of the aromatic rings of the solvent in the first solvation layer.

Now that it is shown that the exfoliation process is enthalpy-driven and influenced by both solvent-solvent and solvent-sheet interactions, the question remains as to why ΔH_{sol} follows the order of BD > MET > water, exactly the same as the molecular weight of the solvent molecules? To

investigate this, the solvent molecules in the first solvation layer of the sheet were identified at 30 ns of the 60 ns simulation, and tracked for the next nanosecond. Here the first solvation layer is defined as solvent molecules whose COM is within 0.5 nm of the sheet, based on the solvent distribution around the sheet (SI, Section S4). Simulation snapshots in SI Section S4 shows that as the solvent size increases, the molecules in the first solvation layer tend to adhere more stably to the sheets. For instance, 80% of the initially adhering BD molecules remain in the first solvation layer while the corresponding number is only 5% for water. Similar observations are made in the US simulations for two nanosheets (SI, Section S4), where after the first 1 ns 82%, 17%, and 5% of the solvent molecules remain in the first solvation layer, respectively for BD, MET, and water. Water behaves much more dynamically, and there are frequent exchanges between water molecules on the interface and those in the bulk. In contrast, the larger MET and especially BD molecules can maintain their positions around and even between the sheets (SI, Section S4). Their lower mobility near the sheet and less exchange with the bulk are consistent with the higher value of $|\Delta H_{sol}|$, suggesting more stably established vdW and electrostatic interaction between the sheet and the solvent.

3.3.2. Group 2 (solvents with carbonyl group)

Similar to group 1, solvent molecules in group 2 are also linear molecules with polar groups (albeit different) capable of forming H-bonds. It is therefore not surprising that the result of ΔG_{exf} and ΔG_{sol} for these two groups show similar behaviors, and data in Figure 3b for all solvents in these two groups form a single class that can be clearly distinguished from group 3. Analysis in SI Section S5 shows that solvation of the g-C_3N_4 nanosheet in group 2 solvents is also driven by enthalpy. The $T\Delta S_{sol}$ (< 0) term is in the same range for all three solvents; ΔH_{sol} (< 0) for ACE and FRM is close, while the magnitude of ΔH_{sol} is much larger for DMF. Consequently, DMF also has the highest $|\Delta G_{sol}|$ and lowest ΔG_{exf}. Considering data from groups 1 and 2 together in Figure 3, DMF stands out as the solvent with the best potential to exfoliate g-C_3N_4 nanosheets.

Unlike group 1, the ranking of $|\Delta G_{sol}|$ in group 2 does not follow the order of the MW of the solvent molecules. In particular, FRM has a smaller MW (45.0) than ACE (58.1), yet the two solvents have similar $|\Delta G_{sol}|$. Considering groups 1 and 2 together, BD has larger MW than DMF, yet its $|\Delta G_{sol}|$ is lower. Therefore, it appears that when the solvent molecules possess a carbonyl group, their interaction with the sheet is not directly correlated with their size. The radial distribution

function (RDF, g(r)) of the solvent oxygen around N atoms of the sheet is shown in SI Section S6 for all solvents in groups 1 and 2, based on the last 30 ns of the 60 ns simulations. The location of the first peak (r_p) in each curve corresponds to the accumulation of the solvent oxygen near the N atoms of the sheet in the first hydration layer. A negative correlation is observed between r_p and $|\Delta G_{sol}|$ (Figure 4b). In other words, solvents that can orient their oxygen closer to the surface of the sheet tend to have a higher $|\Delta G_{sol}|$. Among the solvents from groups 1 and 2, DMF has the lowest value of r_p. One possible reason could be the partial atomic charge of the solvent oxygen, which is shown in inset of Figure 4b. The charge is most negative for water oxygen and least negative for DMF. Since the nitrogen atoms on the g-C_3N_4 nanosheet also carry a negative partial charge (-0.35), less negative charge of the solvent oxygen can alleviate their local repulsion with the nitrogen, allowing other attractive interactions (vdW, electrostatic force between atoms with opposing partial atomic charges) to be more stably established.

In Section 3.3.1, it is discussed that $|\Delta G_{sol}|$ does not have a direct correlation with the number of H-bonds broken and formed during the solvation; rather it is related to the mobility of the solvent molecules around the sheet. This motivates us to investigate the persistence of the solvent around the sheet by calculating the lifetime of the H-bonds between them, through the following autocorrelation function [59]:

$$C(\tau) = < s_i(t)\, s_i(t+\tau) > \quad (6)$$

Here $s_i(t)$ indicates whether H-bond i is present (s_i = 1) or absent (s_i = 0) at time t, and $< \bullet >$ performs an average over all time t and all H-bonds i between the solvent and the sheet. The integral $\int_0^\infty C(\tau)d\tau$ gives a rough estimate of the average H-bond lifetime, which is shown in Figure 4b for group 1 and 2 solvents. Interestingly, the average H-bond lifetime follows an almost linear relationship with $|\Delta G_{sol}|$. Consistent with the visual observations in SI Section S4 this result confirms that higher magnitude of $|\Delta G_{sol}|$ is associated with less mobility and more stable adherence of the solvent molecules around the sheet.

3.3.3. Group 3 (solvents with aromatic structures):

Group 3 solvents have a distinct structure compared with group 1 and 2 solvents, containing a ring-like, instead of linear, structure. Their ΔG_{exf} vs. $|\Delta G_{sol}|$ data are separated from the other two groups in Figure 3b, and within similar range of $|\Delta G_{sol}|$ this group tends to have lower ΔG_{exf}. Energetics

analysis in SI Section S5 shows that the solvation of the g-C_3N_4 nanosheet in group 3 solvent is still enthalpy-driven. Since these solvents contain aromatic structures, it is of interest to study potential π-π interactions between solvent molecules and the sheet. Previous DFT simulations investigated the adsorption of ionic liquid on BN nanosheets [60], and reported the presence of π–π, CH-π, and anion–π interactions. π-π interactions between two aromatic rings are typically manifested by a small separation (less than 5.0 Å [61]) between them [62]. SI Section S6 provides the RDFs of the center of the aromatic ring around the carbon and nitrogen atoms on the sheet (data based on last 30 ns of the 60 ns simulations from the last set of simulations in Table 1). The curves corresponding to different solvents almost overlap, demonstrating similar distribution of the aromatic ring around the sheet. The location of the first RDF peak is 4.2 Å for carbon and 3.8 Å for nitrogen, suggesting that the aromatic centers are positioned slightly closer to the nitrogen atoms. To measure the relative orientation of the solvent aromatic rings with respect to the sheet, Figure 4c shows the probability distribution of the angle between the normal of the aromatic rings in the solvents and the normal of the solvated sheet. Here the solvent molecules considered are in the first solvation layer and the probability distribution is generated based on last 30 ns of the 60 ns simulation. For all three solvents most of the molecules have an angle > 80°, corresponding to nearly perpendicular orientation relative to the sheets. NMP, however, has a higher probability of acquiring smaller angles (< 10°) than the other two solvents. This suggests that while all solvents experience T-shaped π-π interactions [63] with the sheet, NMP benefits from having more offset-stacked (parallel-displaced) [64]. This conformation in turn promotes the solvent-sheet interactions and makes NMP a better medium for LPE (highest $|\Delta G_{sol}|$ and lowest ΔG_{exf} in this group).

3.4. Discussion

3.4.1. Mobility of solvent molecules around nanosheet

In sections 3.3.1 and 3.3.2, an interesting correlation is observed between $|\Delta G_{sol}|$ and the mobility of the linear solvent molecules around the sheet. Here the analysis is extended to solvents in all three groups. For each 60 ns simulation where a single nanosheet was equilibrated in a solvent, the solvent molecules in the first solvation layer at t = 25 ns were tracked till the end of the simulation. The fraction of these molecules that departed from the first solvation layer (M) was calculated as a function of time and presented in SI Section S7. M starts from zero and increases with time,

reaching a plateau at t = 50 ns for all solvents. The average from the last 10 ns (50 to 60 ns), denoted by M_{ave}, is shown in Figure 5a by plotting $\ln(M_{ave})$ against $|\Delta G_{sol}|/kT$, where k is the Boltzmann constant. All data fall near a straight line, suggesting the following relationship between M_{ave} and $|\Delta G_{sol}|$:

$$M_{ave} = \mathrm{A}\, e^{\frac{-a|\Delta G_{sol}|}{kT}} \quad (7)$$

where A and $a > 0$ are constants. This is a relationship that resembles the Arrhenius equation [65], with $|\Delta G_{sol}|$ serving the role of an activation energy that is required to drive the molecules to depart from the first solvation layer and diffuse into the bulk.

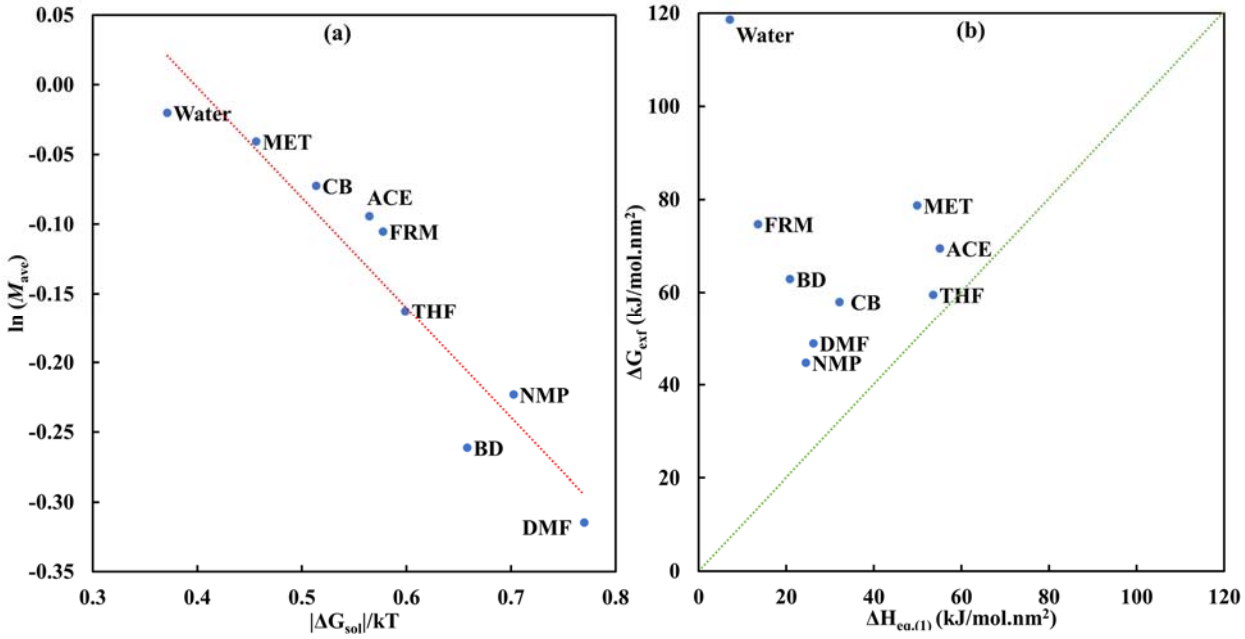

Figure 5. (a) $\ln(M_{ave})$ versus $\frac{|\Delta G_{sol}|}{kT}$ for all the solvents studied in this work. (b) Comparison of $\Delta H_{eq.(1)}$ and ΔG_{exf} from this study.

3.4.2. Implications for LPE

Previous studies [29] have reported that the concentration of the as-obtained g-C_3N_4 nanosheets in suspension was extremely low (less than 3 mg/mL). Fabricating graphene-like g-C_3N_4 with a single atomic layer in a relatively high concentration remains a strenuous task since the g-C_3N_4 nanosheets tend to aggregate due to their high surface energy [66]. Hence, a key goal of the studies on LPE is to find the most suitable dispersant–solvent system that can generate uniform and stable dispersion of g-C_3N_4 sheets with high concentration. Smaller values of ΔG_{exf} correspond to less

amount of energy required to separate aggregated sheets, as well as less tendency for the sheets to aggregate [57]. It is therefore expected that the concentration of dispersed g-C_3N_4 sheets can reach higher values in the solvents with lower ΔG_{exf}, which has been verified experimentally for graphene solvated in ionic solvents [67]. Our results showed that NMP, DMF, CB, and THF have the lowest ΔG_{exf}, therefore they are predicted to be better media for LPE. This is in line with the experiments by Yang et al. where g-C_3N_4 nanosheets were found to be more stably dispersed in NMP and IPA among five solvents (NMP, IPA, water, ACE, and ethanol) [28]. It should be noted that NMP has a high boiling point and is challenging to be removed in order to obtain exfoliated g-C_3N_4 nanosheets. The evaporation process is slow and aggregation of exfoliated nanosheets may occur during the process [28]. This provides quantitative and molecular-level support for why DMF is widely used as an effective exfoliation medium in experimental studies [28,68–72].

In drastic contrast to NMP and DMF, water has a very large ΔG_{exf}, 52% higher than the second poorest solvent (MET) in this study. $|\Delta G_{sol}|$ of water is also the lowest, about 23% smaller than the next in line (MET). This suggests low affinity of water molecules to g-C_3N_4 sheets, which is manifested through its lowest average H-bond lifetime, furthest distribution from the sheet (largest r_p value), and highest molecular mobility in the adsorption layer. Based on the data, water is not a suitable candidate for the LPE of g-C_3N_4. The predicted poor performance of water is in line with experimental studies where a relatively low concentration of dispersed g-C_3N_4 sheets was found in water [29,31]. Recognizing the advantages of water being a solvent (e.g., safe, abundant, easily accessible), surface modifications of g-C_3N_4 sheets may be considered to enhance their interactions with water and increase their aqueous dispersibility.

Sresht et al. investigated the LPE of phosphorene sheets using MD simulations [44]. It was discussed that the performance of a solvent depended on its molecular shape, and solvents with a planar structure, such as NMP and dimethyl sulfoxide, behave like molecular wedges that can intercalate more efficiently [44]. In agreement with this, our data show that for similar $|\Delta G_{sol}|$, group 3 solvents with planar structures tend to have smaller ΔG_{exf}. More interestingly, our results have repeatedly shown a correlation between ΔG_{exf} and the mobility of solvent molecules around the nanosheet. For example, for DMF, NMP, and BD, up to 30% of the solvents in the first solvation layer lingered near the sheet even after 35 ns (SI Section S7). Those solvent molecules essentially formed an adsorption layer on the nanosheet, which could shield the sheet-sheet

interactions, potentially hindering the aggregation and allowing stable dispersion of individual sheets. Based on our observations, several suggestions can be made that might promote the stability of the adsorption layer. Firstly, highly negative partial atomic charges (typically related to high polarity) should be avoided, so as to reduce the repulsion with the electronegative nitrogen on the sheet. Secondly, solvents with larger size (higher MW) present an advantage. Finally, solvents with an aromatic structure are preferred, especially those that are able to form more parallel π-π stacked conformations.

Energetics analysis in this work has demonstrated enthalpy as the main driving force in the solvation of g-C_3N_4. While the dominance of enthalpy has been reported in the literature for the solvation of long-chain polymers [73,74], to our knowledge this is the first time it is reported for 2D materials. Coleman et al. [22] proposed a first-order estimation, eq. (1), for the enthalpy of mixing of graphene as an approximation for the free energy of exfoliation. . To examine the validity of this approximation for g-C_3N_4, we used $\emptyset = \frac{V_{sheet}}{V_{mix}}$ to rewrite eq. (1) into

$$\Delta H_{\text{eq.(1)}} \equiv \frac{\Delta H_{mix}\, T_{sheet}}{V_{sheet}} = 2\left(\sqrt{E_{sur}^{sheet}} - \sqrt{E_{sur}^{solvent}}\right)^2$$

which represents the enthalpy of mixing per unit area of the sheet. $\Delta H_{\text{eq.(1)}}$ was calculated using the surface energy values from Tables S2 and S3, respectively for E_{sur}^{sheet} and $E_{sur}^{solvent}$, and compared with ΔG_{exf} from our work (Figure 5b). For all of the solvents, $\Delta H_{\text{eq.(1)}}$ underestimates ΔG_{exf} and the discrepancy is particularly large for solvents with high surface tension (such as water and FRM). The ranking of $\Delta H_{\text{eq.(1)}}$ follows: ACE > THF > MET > CB > DMF > NMP > BD > FRM > water. If $\Delta H_{\text{eq.(1)}}$ were to be used to select the solvent for LPE, then water would be chosen as the best solvent among these nine solvents. This is in contradiction with our earlier discussion on the performance of water in LPE. Therefore, eq. (1) is a poor estimation for the free energy of exfoliation for g-C_3N_4 and should not be used as a selection criterion.

4. Conclusion

In this study, MD simulations are performed along with extensive potential of mean force (PMF) calculations, to evaluate the free energy of exfoliation of g-C_3N_4 nanosheets in nine common solvents. The solvation free energy of a single g-C_3N_4 nanosheet is also calculated and compared with the free energy of exfoliation of two g-C_3N_4 nanosheets in the same solvent. The effect of

structural properties of solvents on the free energy cost of the exfoliation process is analyzed. Our results show that similar to other 2D materials such as BN [46] and graphene [47], the most probable path for the exfoliation of g-C_3N_4 nanosheets is in the parallel (shear) direction. Based on PMF calculations, the performance of the nine solvents in exfoliating or dispersing g-C_3N_4 sheets is ranked, with the best solvents being NMP, DMF, CB, and THF. This provides quantitative and molecular-level support for why NMP and DMF are widely used as exfoliation media in experimental studies [28,68–72]. A high correlation is found between the free energy of exfoliation of two sheets and the solvation free energy of a single sheet, with higher magnitude of solvation free energy corresponding to lower free energy of exfoliation. Regardless of the molecular structure of the solvents, the solvation of g-C_3N_4 sheet is driven primarily by enthalpy. Analysis of the first solvation layer shows that solvents with higher magnitude of solvation free energy tend to be less mobile in this layer, and in some cases a stable adsorption layer is formed around the sheet. Additionally, our results show that the first-order estimation for the free energy of exfoliation proposed by Coleman et al. [22] is insufficient and can lead to large errors especially for water.

To our best knowledge, this is the first atomistic-level study that determines a quantitative relationship between solvent properties and the performance of liquid phase exfoliation. Not only have the simulations been able to provide explanations for solvent selection in some experiments [28,68–72], they have also generated critical insights into the underlying mechanisms which are not accessible by experiments. Also, through several novel analyses, we have for the first time revealed key factors that govern the efficacy of the solvent. This has allowed us to propose a comprehensive set of principles for the selection and design of effective solvents in liquid phase exfoliation of g-C_3N_4, including less negative partial atomic charges, higher molecular weight and the presence of aromatic structures.

Several future directions are recognized. First, in the literature there are two main molecular structures proposed for g-C_3N_4 nanosheets: heptazine based and *s*-triazine based [26]. Here, we only considered the former and it is of interest to investigate the latter structure. It is also worth studying whether the geometry of the model (e.g., triangle in this work vs. other shapes) affects the free energy results. Second, there exist many other solvents with structural features different from those studied in this work. Extending the present framework to a large number of solvents

may allow for a more general model to be established that can predict the free energy of exfoliation. Lastly, future work can be conducted to relate the free energy of exfoliation to critical concentrations of delaminated g-C_3N_4 in a solvent that lead to aggregation and precipitation [29].

Supporting Information

Effect of sheet size; Validation of force field parameters; Additional data from pulling and US simulations; Additional analysis for group 1; Energy analysis for the solvation process; Radial distribution function (RDF) plots; Fraction of molecules that departed from the first solvation layer

Acknowledgement

Compute Canada is gratefully acknowledged for providing the computing resources and technical support. TT acknowledges financial support from the Natural Sciences and Engineering Research Council of Canada (NSERC; Grant numbers: RGPIN-2018-04281, RGPAS-2018-522655). KS thanks NSERC for financial support (Grant number: RGPIN-2020-04620).

References

[1] J. Fu, J. Yu, C. Jiang, B. Cheng, g-C3N4-Based Heterostructured Photocatalysts, Adv Energy Mater. (2018). https://doi.org/10.1002/aenm.201701503.

[2] X. Ma, J. Hu, H. He, S. Dong, C. Huang, X. Chen, New Understanding on Enhanced Photocatalytic Activity of g-C3N4/BiPO4 Heterojunctions by Effective Interfacial Coupling, ACS Appl Nano Mater. 1 (2018) 5507–5515. https://doi.org/10.1021/acsanm.8b01012.

[3] Y. Yuan, L. Zhang, J. Xing, M.I.B. Utama, X. Lu, K. Du, Y. Li, X. Hu, S. Wang, A. Genç, R. Dunin-Borkowski, J. Arbiol, Q. Xiong, High-yield synthesis and optical properties of g-C3N4, Nanoscale. 7 (2015) 12343–12350. https://doi.org/10.1039/c5nr02905h.

[4] J. Xu, L. Zhang, R. Shi, Y. Zhu, Chemical exfoliation of graphitic carbon nitride for efficient heterogeneous photocatalysis, J Mater Chem A Mater. 1 (2013) 14766–14772. https://doi.org/10.1039/C3TA13188B.

[5] Y. Liu, D. Xie, M. Song, L. Jiang, G. Fu, L. Liu, J. Li, Water desalination across multilayer graphitic carbon nitride membrane: Insights from non-equilibrium molecular dynamics simulations, Carbon N Y. 140 (2018) 131–138. https://doi.org/10.1016/j.carbon.2018.08.043.

[6] A. Alaghmandfard, K. Ghandi, A Comprehensive Review of Graphitic Carbon Nitride (g-C3N4)–Metal Oxide-Based Nanocomposites: Potential for Photocatalysis and Sensing, Nanomaterials 2022, Vol. 12, Page 294. 12 (2022) 294. https://doi.org/10.3390/NANO12020294.

[7] Y. Dong, Q. Wang, H. Wu, Y. Chen, C.H. Lu, Y. Chi, H.H. Yang, Graphitic Carbon Nitride Materials: Sensing, Imaging and Therapy, Small. 12 (2016) 5376–5393. https://doi.org/10.1002/SMLL.201602056.

[8] S. Patnaik, D.P. Sahoo, K. Parida, An overview on Ag modified g-C3N4 based nanostructured materials for energy and environmental applications, Renewable and Sustainable Energy Reviews. 82 (2018) 1297–1312. https://doi.org/10.1016/J.RSER.2017.09.026.

[9] Y. Wang, L. Liu, T. Ma, Y. Zhang, H. Huang, Y.H. Wang, L.Z. Liu, Y.H. Zhang, H.W. Huang, T.Y. Ma, 2D Graphitic Carbon Nitride for Energy Conversion and Storage, Adv Funct Mater. 31 (2021) 2102540. https://doi.org/10.1002/ADFM.202102540.

[10] X. Dong, F. Cheng, Recent development in exfoliated two-dimensional g-C3N4 nanosheets for photocatalytic applications, J Mater Chem A Mater. 3 (2015) 23642–23652. https://doi.org/10.1039/c5ta07374j.

[11] S. Cao, J. Low, J. Yu, M. Jaroniec, Polymeric Photocatalysts Based on Graphitic Carbon Nitride, Advanced Materials. 27 (2015) 2150–2176. https://doi.org/10.1002/adma.201500033.

[12] Y. Zheng, L. Lin, B. Wang, X. Wang, Graphitic Carbon Nitride Polymers toward Sustainable Photoredox Catalysis, Angewandte Chemie International Edition. 54 (2015) 12868–12884. https://doi.org/10.1002/anie.201501788.

[13] K.M. Alam, C.E. Jensen, P. Kumar, R.W. Hooper, G.M. Bernard, A. Patidar, A.P. Manuel, N. Amer, A. Palmgren, D.N. Purschke, N. Chaulagain, J. Garcia, P.S. Kirwin, L.C.T. Shoute, K. Cui, S. Gusarov, A.E. Kobryn, V.K. Michaelis, F.A. Hegmann, K. Shankar, Photocatalytic Mechanism Control and Study of Carrier Dynamics in CdS@C3N5Core-Shell Nanowires, ACS Appl Mater Interfaces. 13 (2021) 47418–47439. https://doi.org/10.1021/ACSAMI.1C08550/ASSET/IMAGES/LARGE/AM1C08550_0011.JPEG.

[14] S. Angizi, M. Ali Akbar, M. Darestani-Farahani, al -, S. Dhanraj Nehate, S. Sundaresh, R. Peale, P. Kumar, S. Mulmi, D. Laishram, K.M. Alam, U.K. Thakur, V. Thangadurai, K. Shankar, Water-splitting photoelectrodes consisting of heterojunctions of carbon nitride with a p-type low bandgap double perovskite oxide, Nanotechnology. 32 (2021) 485407. https://doi.org/10.1088/1361-6528/ABEDEC.

[15] S. Cao, H. Chen, F. Jiang, Z. Hu, X. Wang, Construction of Acetaldehyde-Modified g-C 3 N 4 Ultrathin Nanosheets via Ethylene Glycol-Assisted Liquid Exfoliation for Selective Fluorescence Sensing of Ag +, ACS Appl Mater Interfaces. 10 (2018) 44624–44633. https://doi.org/10.1021/ACSAMI.8B15501/ASSET/IMAGES/LARGE/AM-2018-15501V_0002.JPEG.

[16] B. Abreu, B. Almeida, P. Ferreira, R. M. F. Fernandes, D.M. Fernandes, E.F. Marques, A critical assessment of the role of ionic surfactants in the exfoliation and stabilization of 2D nanosheets: The case of the transition metal dichalcogenides MoS2, WS2 and MoSe2, J Colloid Interface Sci. 626 (2022) 167–177. https://doi.org/10.1016/J.JCIS.2022.06.097.

[17] H. Zhao, H. Wu, J. Wu, J. Li, Y. Wang, Y. Zhang, H. Liu, Preparation of MoS2/WS2 nanosheets by liquid phase exfoliation with assistance of epigallocatechin gallate and study as an additive for high-performance lithium-sulfur batteries, J Colloid Interface Sci. 552 (2019) 554–562. https://doi.org/10.1016/J.JCIS.2019.05.080.

[18] Q. Wan, H. Wang, S. Li, J. Wang, Efficient liquid-phase exfoliation of few-layer graphene in aqueous 1, 1, 3, 3-tetramethylurea solution, J Colloid Interface Sci. 526 (2018) 167–173. https://doi.org/10.1016/J.JCIS.2018.04.110.

[19] C. Huo, Z. Yan, X. Song, H. Zeng, 2D materials via liquid exfoliation: a review on fabrication and applications, Sci Bull (Beijing). 60 (2015) 1994–2008. https://doi.org/10.1007/S11434-015-0936-3.

[20] M. Inagaki, T. Tsumura, T. Kinumoto, M. Toyoda, Graphitic carbon nitrides (g-C3N4) with comparative discussion to carbon materials, Carbon N Y. 141 (2019) 580–607. https://doi.org/10.1016/J.CARBON.2018.09.082.

[21] Y. Hernandez, M. Lotya, D. Rickard, S.D. Bergin, J.N. Coleman, Measurement of multicomponent solubility parameters for graphene facilitates solvent discovery, Langmuir. 26 (2010) 3208–3213. https://doi.org/10.1021/la903188a.

[22] J.N. Coleman, M. Lotya, A. O'Neill, S.D. Bergin, P.J. King, U. Khan, K. Young, A. Gaucher, S. De, R.J. Smith, I. v. Shvets, S.K. Arora, G. Stanton, H.Y. Kim, K. Lee, G.T. Kim, G.S. Duesberg, T. Hallam, J.J. Boland, J.J. Wang, J.F. Donegan, J.C. Grunlan, G. Moriarty, A. Shmeliov, R.J. Nicholls, J.M. Perkins, E.M. Grieveson, K. Theuwissen, D.W. McComb, P.D. Nellist, V. Nicolosi, Two-dimensional nanosheets produced by liquid exfoliation of layered materials, Science (1979). 331 (2011) 568–571. https://doi.org/10.1126/SCIENCE.1194975.

[23] L. Ma, H. Fan, J. Wang, Y. Zhao, H. Tian, G. Dong, Water-assisted ions in situ intercalation for porous polymeric graphitic carbon nitride nanosheets with superior photocatalytic hydrogen evolution performance, Appl Catal B. 190 (2016) 93–102. https://doi.org/10.1016/j.apcatb.2016.03.002.

[24] C. Wu, S. Xue, Z. Qin, M. Nazari, G. Yang, S. Yue, T. Tong, H. Ghasemi, F.C.R. Hernandez, S. Xue, D. Zhang, H. Wang, Z.M. Wang, S. Pu, J. Bao, Making g-C3N4 ultra-thin nanosheets active for photocatalytic overall water splitting, Appl Catal B. 282 (2021) 119557. https://doi.org/10.1016/j.apcatb.2020.119557.

[25] S.P. Pattnaik, A. Behera, S. Martha, R. Acharya, K. Parida, Facile synthesis of exfoliated graphitic carbon nitride for photocatalytic degradation of ciprofloxacin under solar irradiation, J Mater Sci. 54 (2019) 5726–5742. https://doi.org/10.1007/s10853-018-03266-x.

[26] W.J. Ong, L.L. Tan, Y.H. Ng, S.T. Yong, S.P. Chai, Graphitic Carbon Nitride (g-C3N4)-Based Photocatalysts for Artificial Photosynthesis and Environmental Remediation: Are We a Step Closer to Achieving Sustainability?, Chem Rev. 116 (2016) 7159–7329. https://doi.org/10.1021/acs.chemrev.6b00075.

[27] M. Ayán-Varela, S. Villar-Rodil, J.I. Paredes, J.M. Munuera, A. Pagán, A.A. Lozano-Pérez, J.L. Cenis, A. Martínez-Alonso, J.M.D. Tascón, Investigating the Dispersion Behavior in Solvents, Biocompatibility, and Use as Support for Highly Efficient Metal Catalysts of Exfoliated Graphitic Carbon Nitride, ACS Appl Mater Interfaces. 7 (2015) 24032–24045. https://doi.org/10.1021/acsami.5b06974.

[28] S. Yang, Y. Gong, J. Zhang, L. Zhan, L. Ma, Z. Fang, R. Vajtai, X. Wang, P.M. Ajayan, Exfoliated graphitic carbon nitride nanosheets as efficient catalysts for hydrogen evolution under visible light, Advanced Materials. 25 (2013) 2452–2456. https://doi.org/10.1002/adma.201204453.

[29] Q. Lin, L. Li, S. Liang, M. Liu, J. Bi, L. Wu, Efficient synthesis of monolayer carbon nitride 2D nanosheet with tunable concentration and enhanced visible-light photocatalytic activities, Appl Catal B. 163 (2015) 135–142. https://doi.org/10.1016/j.apcatb.2014.07.053.

[30] J.N. Coleman, M. Lotya, A. O'Neill, S.D. Bergin, P.J. King, U. Khan, K. Young, A. Gaucher, S. De, R.J. Smith, I. v. Shvets, S.K. Arora, G. Stanton, H.Y. Kim, K. Lee, G.T. Kim, G.S. Duesberg, T. Hallam, J.J. Boland, J.J. Wang, J.F. Donegan, J.C. Grunlan, G. Moriarty, A. Shmeliov, R.J. Nicholls, J.M. Perkins, E.M. Grieveson, K. Theuwissen, D.W. McComb, P.D. Nellist, V. Nicolosi, Two-dimensional nanosheets produced by liquid exfoliation of layered materials, Science (1979). 331 (2011) 568–571. https://doi.org/10.1126/science.1194975.

[31] X. Zou, Y. Zhao, M. Li, S. Zhou, C. Chen, Construction of graphitic carbon nitride nanosheets via an improved solvent exfoliation strategy and interfacial mechanics insight from molecular dynamics simulations, Journal of Porous Materials. 28 (2021) 943–954. https://doi.org/10.1007/s10934-021-01047-7.

[32] Y. Zhang, C. Shen, X. Lu, X. Mu, P. Song, Effects of defects in g-C3N4 on excited-state charge distribution and transfer: Potential for improved photocatalysis, Spectrochim Acta A Mol Biomol Spectrosc. 227 (2020) 117687. https://doi.org/10.1016/J.SAA.2019.117687.

[33] X. Zhou, M. Zhu, L. Kang, Single-Atom X/g-C3N4(X = Au1, Pd1, and Ru1) Catalysts for Acetylene Hydrochlorination: A Density Functional Theory Study, Catalysts 2019, Vol. 9, Page 808. 9 (2019) 808. https://doi.org/10.3390/CATAL9100808.

[34] X. Chen, R. Hu, DFT-based study of single transition metal atom doped g-C3N4 as alternative oxygen reduction reaction catalysts, Int J Hydrogen Energy. 44 (2019) 15409–15416. https://doi.org/10.1016/J.IJHYDENE.2019.04.057.

[35] Z. Bonakchi, A. Nakhaei Pour, S. Soheili, Molecular simulation of methane on various g-C3N4 isomers: collision, adsorption, desorption, and diffusion studies, Journal of the Iranian Chemical Society. 19 (2022) 3649–3657. https://doi.org/10.1007/S13738-022-02562-3/TABLES/2.

[36] L. Kang, M. Zhu, Y. Zhao, A DFT Study of Acetylene Hydrogenation Catalyzed by S-Doped Pd 1 /g-C 3 N 4, (n.d.). https://doi.org/10.3390/catal9110887.

[37] B. Kumru, M. Antonietti, B.V.K.J. Schmidt, Enhanced Dispersibility of Graphitic Carbon Nitride Particles in Aqueous and Organic Media via a One-Pot Grafting Approach, Langmuir. 33 (2017) 9897–9906. https://doi.org/10.1021/acs.langmuir.7b02441.

[38] W.L. Jorgensen, J. Tirado-Rives, Potential energy functions for atomic-level simulations of water and organic and biomolecular systems, Proc Natl Acad Sci U S A. 102 (2005) 6665–6670. https://doi.org/10.1073/pnas.0408037102.

[39] L.S. Dodda, I.C. De Vaca, J. Tirado-Rives, W.L. Jorgensen, LigParGen web server: An automatic OPLS-AA parameter generator for organic ligands, Nucleic Acids Res. (2017). https://doi.org/10.1093/nar/gkx312.

[40] M. YABE, K. MORI, K. UEDA, M. TAKEDA, Development of PolyParGen Software to Facilitate the Determination of Molecular Dynamics Simulation Parameters for Polymers, Journal of Computer Chemistry, Japan -International Edition. 5 (2019) n/a. https://doi.org/10.2477/jccjie.2018-0034.

[41] L.S. Dodda, J.Z. Vilseck, K.J. Cutrona, W.L. Jorgensen, Evaluation of CM5 Charges for Nonaqueous Condensed-Phase Modeling, J Chem Theory Comput. 11 (2015) 4273–4282. https://doi.org/10.1021/acs.jctc.5b00414.

[42] G.M. Torrie, J.P. Valleau, Nonphysical sampling distributions in Monte Carlo free-energy estimation: Umbrella sampling, J Comput Phys. 23 (1977) 187–199. https://doi.org/10.1016/0021-9991(77)90121-8.

[43] S. Kumar, J.M. Rosenberg, D. Bouzida, R.H. Swendsen, P.A. Kollman, THE weighted histogram analysis method for free-energy calculations on biomolecules. I. The method, J Comput Chem. 13 (1992) 1011–1021. https://doi.org/10.1002/JCC.540130812.

[44] V. Sresht, A.A.H. Pádua, D. Blankschtein, Liquid-Phase Exfoliation of Phosphorene: Design Rules from Molecular Dynamics Simulations, ACS Nano. 9 (2015) 8255–8268. https://doi.org/10.1021/acsnano.5b02683.

[45] A. Gotzias, Binding Free Energy Calculations of Bilayer Graphenes Using Molecular Dynamics, J Chem Inf Model. 61 (2021) 1164–1171. https://doi.org/10.1021/acs.jcim.1c00043.

[46] T.K. Mukhopadhyay, A. Datta, Deciphering the role of solvents in the liquid phase exfoliation of hexagonal boron nitride: A molecular dynamics simulation study, Journal of Physical Chemistry C. 121 (2017) 811–822. https://doi.org/10.1021/acs.jpcc.6b09446.

[47] C. Fu, X. Yang, Molecular simulation of interfacial mechanics for solvent exfoliation of graphene from graphite, Carbon N Y. 55 (2013) 350–360. https://doi.org/10.1016/j.carbon.2012.12.083.

[48] G. Zhou, P. Rajak, S. Susarla, P.M. Ajayan, R.K. Kalia, A. Nakano, P. Vashishta, Molecular Simulation of MoS2 Exfoliation, Sci Rep. 8 (2018) 1–9. https://doi.org/10.1038/s41598-018-35008-z.

[49] C.H. Bennett, Efficient estimation of free energy differences from Monte Carlo data, J Comput Phys. 22 (1976) 245–268. https://doi.org/10.1016/0021-9991(76)90078-4.

[50] M.J. Abraham, T. Murtola, R. Schulz, S. Páll, J.C. Smith, B. Hess, E. Lindah, GROMACS: High performance molecular simulations through multi-level parallelism from laptops to supercomputers, SoftwareX. 1–2 (2015) 19–25. https://doi.org/10.1016/J.SOFTX.2015.06.001.

[51] V. Georgakilas, J.N. Tiwari, K.C. Kemp, J.A. Perman, A.B. Bourlinos, K.S. Kim, R. Zboril, Noncovalent Functionalization of Graphene and Graphene Oxide for Energy Materials, Biosensing, Catalytic, and Biomedical Applications, Chem Rev. 116 (2016) 5464–5519. https://doi.org/10.1021/ACS.CHEMREV.5B00620.

[52] A.M. Silva, M.I. Rojas, Electric and structural properties of polymeric graphite carbon nitride (g-C3N4): A Density Functional Theory study, Comput Theor Chem. (2016). https://doi.org/10.1016/j.comptc.2016.11.004.

[53] B. Mortazavi, Ultra high stiffness and thermal conductivity of graphene like C3N, Carbon N Y. 118 (2017) 25–34. https://doi.org/10.1016/J.CARBON.2017.03.029.

[54] D. Wu, D.A. Kofke, Phase-space overlap measures. II. Design and implementation of staging methods for free-energy calculations, J Chem Phys. 123 (2005) 084109. https://doi.org/10.1063/1.2011391.

[55] H.K. Choi, Y. Oh, H. Jung, H. Hong, B.C. Ku, N.H. You, Y.K. Kim, E.S. Shin, J. Yu, Influences of carboxyl functionalization of intercalators on exfoliation of graphite oxide: A molecular dynamics simulation, Physical Chemistry Chemical Physics. 20 (2018) 28616–28622. https://doi.org/10.1039/c8cp05436c.

[56] H.A. Yu, M. Karplus, A thermodynamic analysis of solvation, J Chem Phys. 89 (1998) 2366. https://doi.org/10.1063/1.455080.

[57] C.J. Shih, S. Lin, M.S. Strano, D. Blankschtein, Understanding the stabilization of liquid-phase-exfoliated graphene in polar solvents: Molecular dynamics simulations and kinetic theory of colloid aggregation, J Am Chem Soc. 132 (2010) 14638–14648. https://doi.org/10.1021/ja1064284.

[58] R. Biswas, Molecular dynamics studies on the exfoliation of graphene in room temperature ionic liquids, J Mol Liq. 337 (2021) 116592. https://doi.org/10.1016/j.molliq.2021.116592.

[59] A. Luzar, D. Chandler, Hydrogen-bond kinetics in liquid water, Nature 1996 379:6560. 379 (1996) 55–57. https://doi.org/10.1038/379055a0.

[60] M. Shakourian-Fard, G. Kamath, Z. Jamshidi, Trends in Physisorption of Ionic Liquids on Boron-Nitride Sheets, (2014). https://doi.org/10.1021/jp506277n.

[61] T. Chen, M. Li, J. Liu, π-π Stacking Interaction: A Nondestructive and Facile Means in Material Engineering for Bioapplications, Cryst Growth Des. 18 (2018) 2765–2783. https://doi.org/10.1021/ACS.CGD.7B01503/ASSET/IMAGES/LARGE/CG-2017-01503A_0004.JPEG.

[62] C.A. Hunter, J.K.M. Sanders, The nature of .pi.-.pi. interactions, J Am Chem Soc. 112 (2002) 5525–5534. https://doi.org/10.1021/JA00170A016.

[63] A.L. Ringer, M.O. Sinnokrot, R.P. Lively, C.D. Sherrill, The effect of multiple substituents on sandwich and T-shaped pi-pi interactions, Chemistry. 12 (2006) 3821–3828. https://doi.org/10.1002/CHEM.200501316.

[64] M. J. Rashkin, M. L. Waters, Unexpected Substituent Effects in Offset π–π Stacked Interactions in Water, J Am Chem Soc. 124 (2002) 1860–1861. https://doi.org/10.1021/ja016508z.

[65] M. Peleg, M.D. Normand, M.G. Corradini, The Arrhenius Equation Revisited, Https://Doi.Org/10.1080/10408398.2012.667460. 52 (2012) 830–851. https://doi.org/10.1080/10408398.2012.667460.

[66] L. Sun, Y. Qi, C.J. Jia, Z. Jin, W. Fan, Enhanced visible-light photocatalytic activity of g-C 3 N 4 /Zn 2 GeO 4 heterojunctions with effective interfaces based on band match, Nanoscale. 6 (2014) 2649–2659. https://doi.org/10.1039/C3NR06104C.

[67] E. Bordes, B. Morcos, D. Bourgogne, J.M. Andanson, P.O. Bussière, C.C. Santini, A. Benayad, M.C. Gomes, A.A.H. Pádua, Dispersion and stabilization of exfoliated graphene in ionic liquids, Front Chem. 7 (2019) 223. https://doi.org/10.3389/FCHEM.2019.00223/BIBTEX.

[68] Y.J. Yuan, Z. Shen, S. Wu, Y. Su, L. Pei, Z. Ji, M. Ding, W. Bai, Y. Chen, Z.T. Yu, Z. Zou, Liquid exfoliation of g-C3N4 nanosheets to construct 2D-2D MoS2/g-C3N4 photocatalyst for enhanced photocatalytic H2 production activity, Appl Catal B. 246 (2019) 120–128. https://doi.org/10.1016/j.apcatb.2019.01.043.

[69] Q. Hao, Y. Song, H. Ji, Z. Mo, X. She, J. Deng, T. Muhmood, X. Wu, S. Yuan, H. Xu, H. Li, Surface N modified 2D g-C 3 N 4 nanosheets derived from DMF for photocatalytic H 2 evolution, Appl Surf Sci. 459 (2018) 845–852. https://doi.org/10.1016/j.apsusc.2018.07.154.

[70] Y. Wang, L. Li, Y. Wei, J. Xue, H. Chen, L. Ding, J. Caro, H. Wang, Water Transport with Ultralow Friction through Partially Exfoliated g-C3N4 Nanosheet Membranes with Self-Supporting Spacers, Angewandte Chemie - International Edition. 56 (2017) 8974–8980. https://doi.org/10.1002/anie.201701288.

[71] Q. Lin, L. Li, S. Liang, M. Liu, J. Bi, L. Wu, Efficient synthesis of monolayer carbon nitride 2D nanosheet with tunable concentration and enhanced visible-light photocatalytic activities, Appl Catal B. 163 (2015) 135–142. https://doi.org/10.1016/j.apcatb.2014.07.053.

[72] L. Ma, H. Fan, M. Li, H. Tian, J. Fang, G. Dong, A simple melamine-assisted exfoliation of polymeric graphitic carbon nitrides for highly efficient hydrogen production from water under visible light, J Mater Chem A Mater. 3 (2015) 22404–22412. https://doi.org/10.1039/C5TA05850C.

[73] K. Koschek, V. Durmaz, O. Krylova, M. Wieczorek, S. Gupta, M. Richter, A. Bujotzek, C. Fischer, R. Haag, C. Freund, M. Weber, J. Rademann, Peptide–polymer ligands for a

tandem WW-domain, an adaptive multivalent protein–protein interaction: lessons on the thermodynamic fitness of flexible ligands, Beilstein Journal of Organic Chemistry 11:93. 11 (2015) 837–847. https://doi.org/10.3762/BJOC.11.93.

[74] F. Jiménez-Ángeles, H.-K. Kwon, K. Sadman, T. Wu, K. R. Shull, M. Olvera de la Cruz, Self-Assembly of Charge-Containing Copolymers at the Liquid–Liquid Interface, ACS Cent Sci. 5 (2019) 688–699. https://doi.org/10.1021/acscentsci.9b00084.